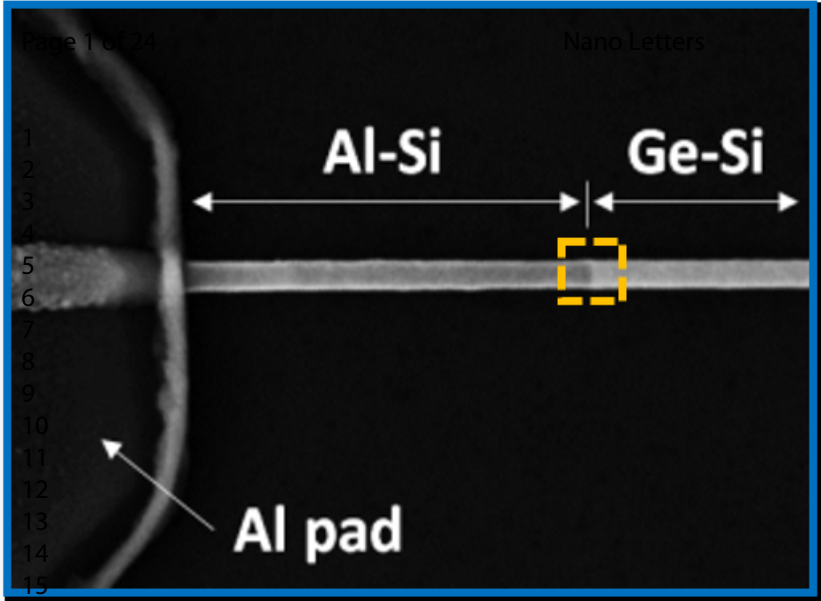

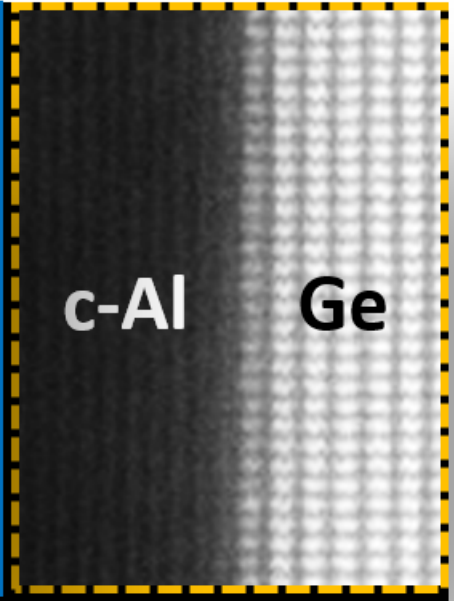

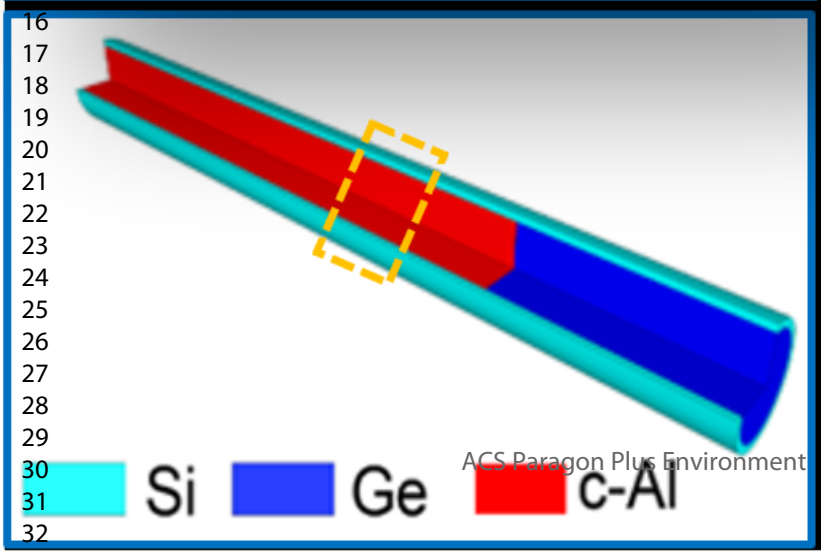

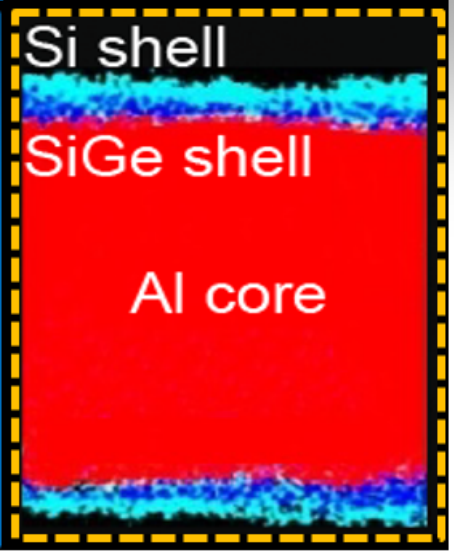

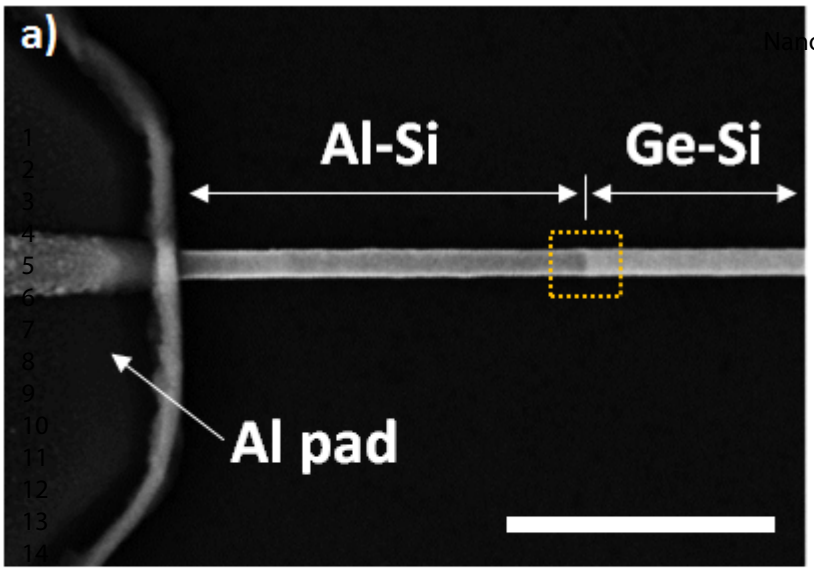

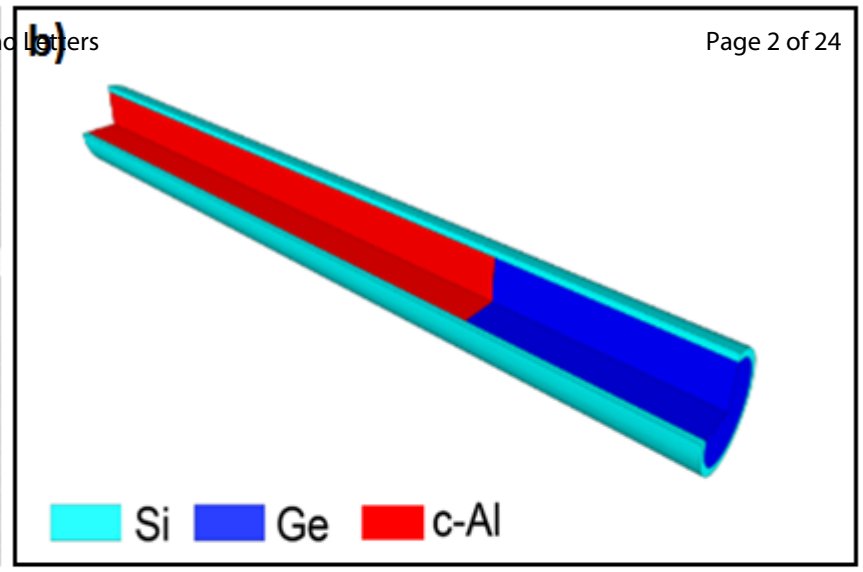

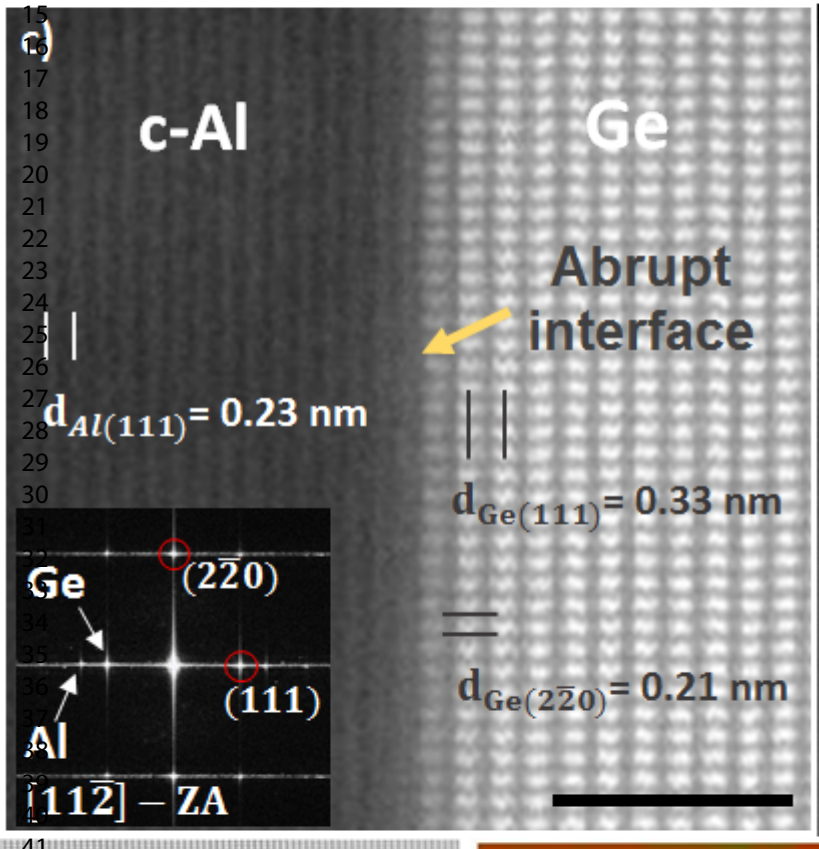

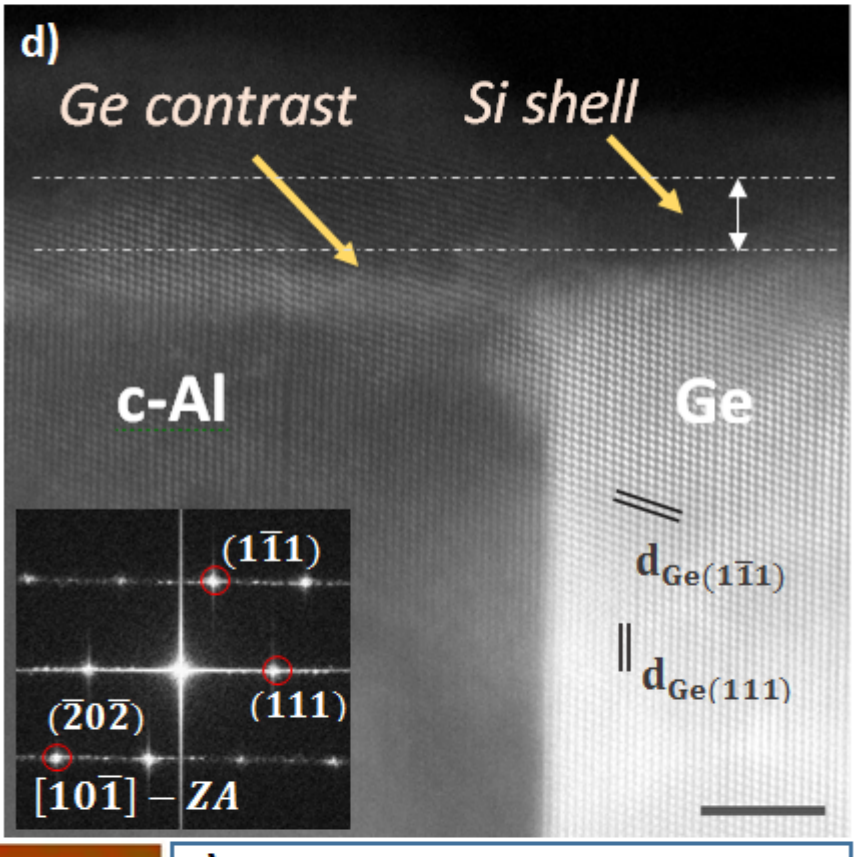

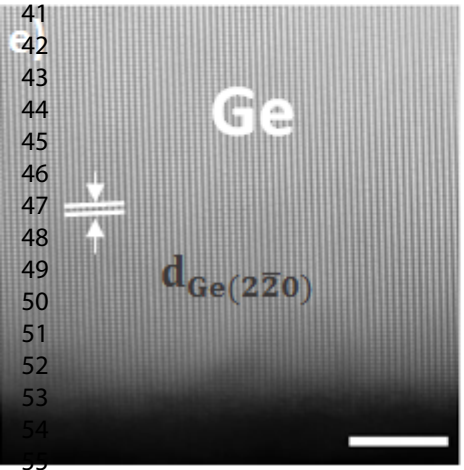

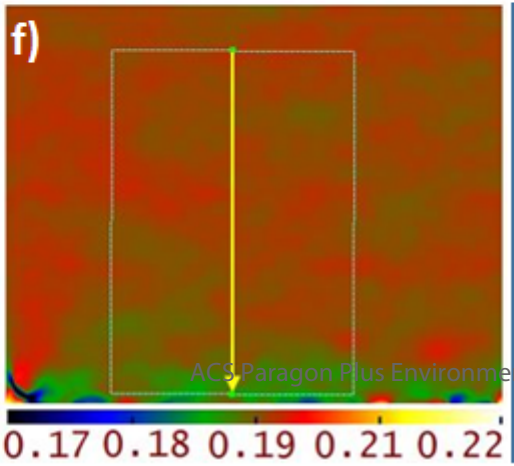

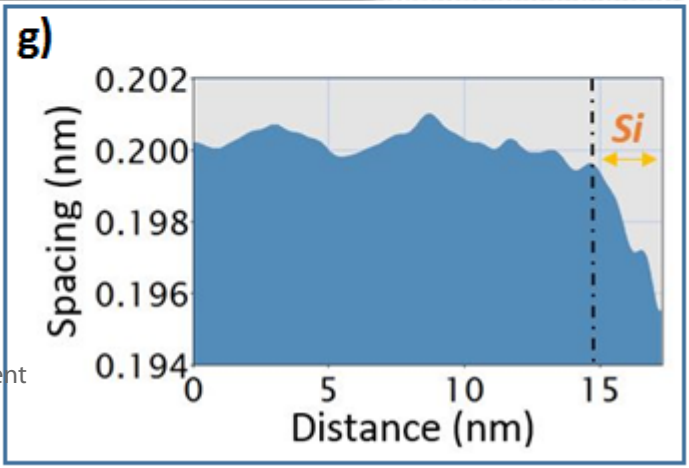

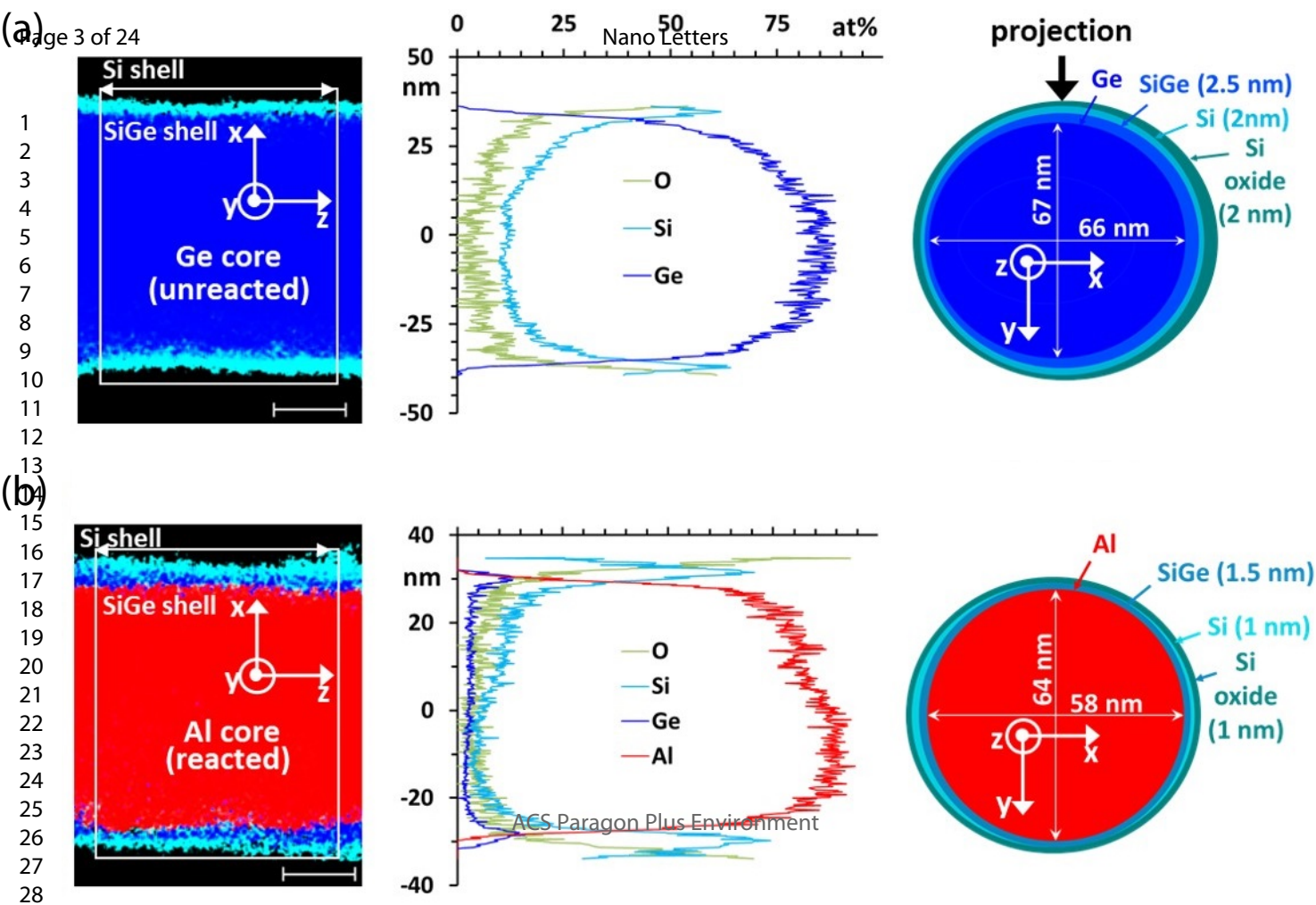

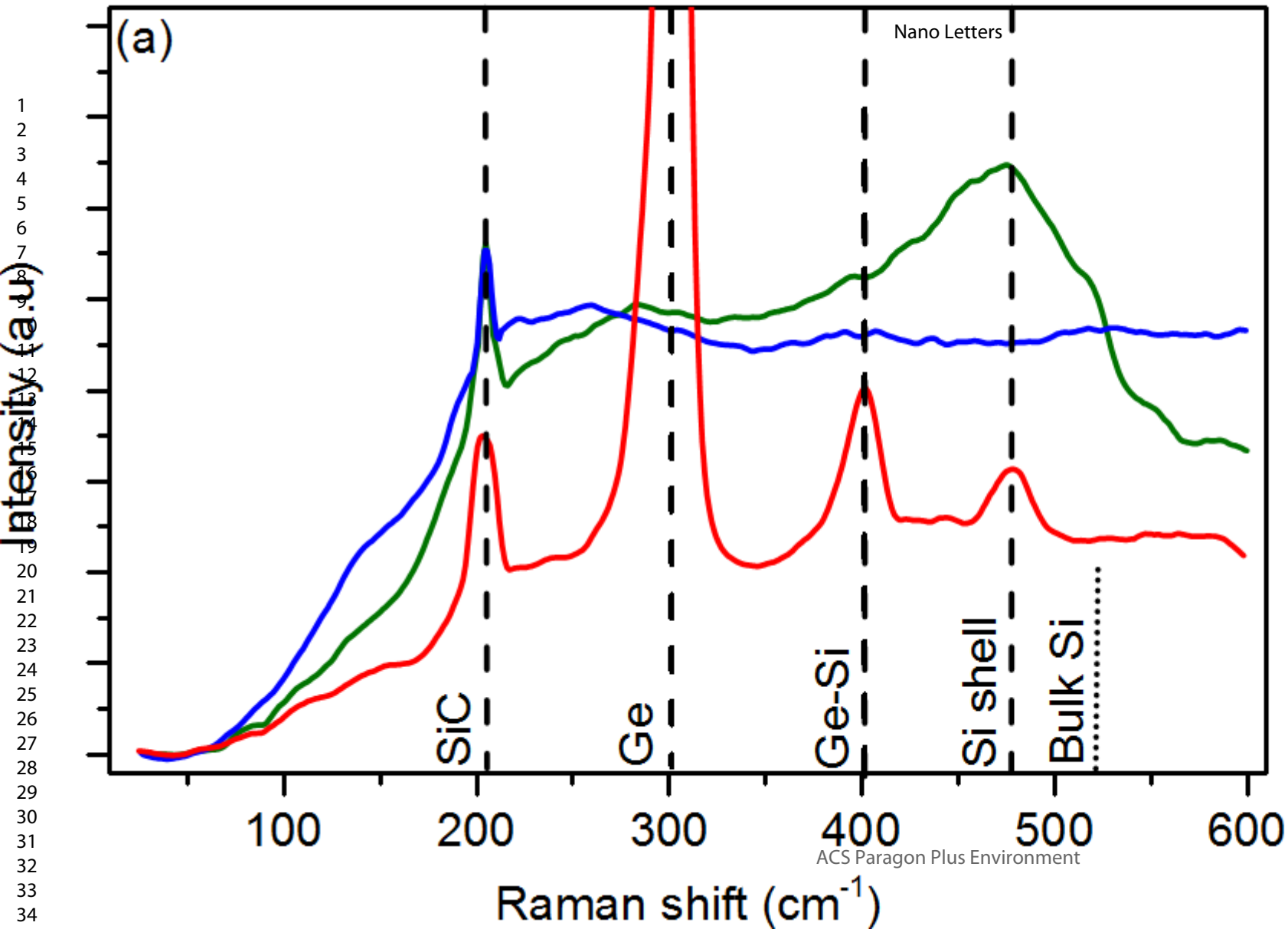
(a)
Intensity (a.u)
SiC
Ge
Ge-Si
Si shell
Bulk Si
100
200
300
400
500
600
Raman shift (cm-1)

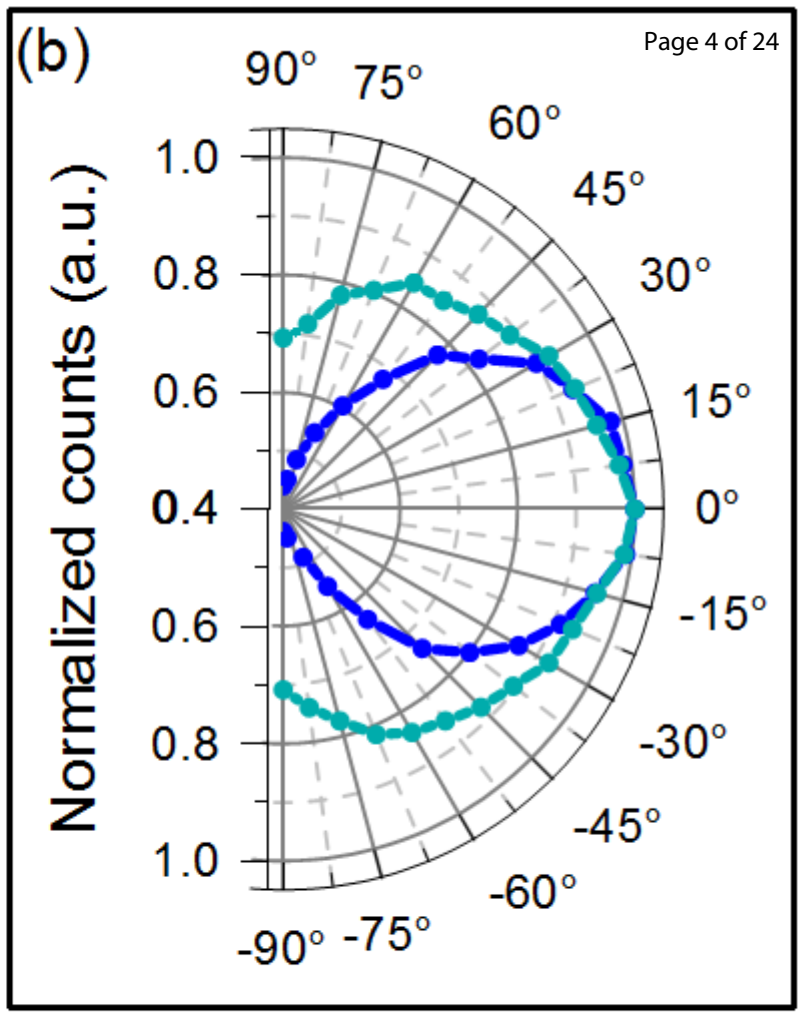
(b)
Normalized counts (a.u.)
90°
75°
60°
45°
30°
15°
0°
-15°
-30°
-45°
-60°
-75°
-90°
1.0
0.8
0.6
0.4
0.6
0.8
1.0

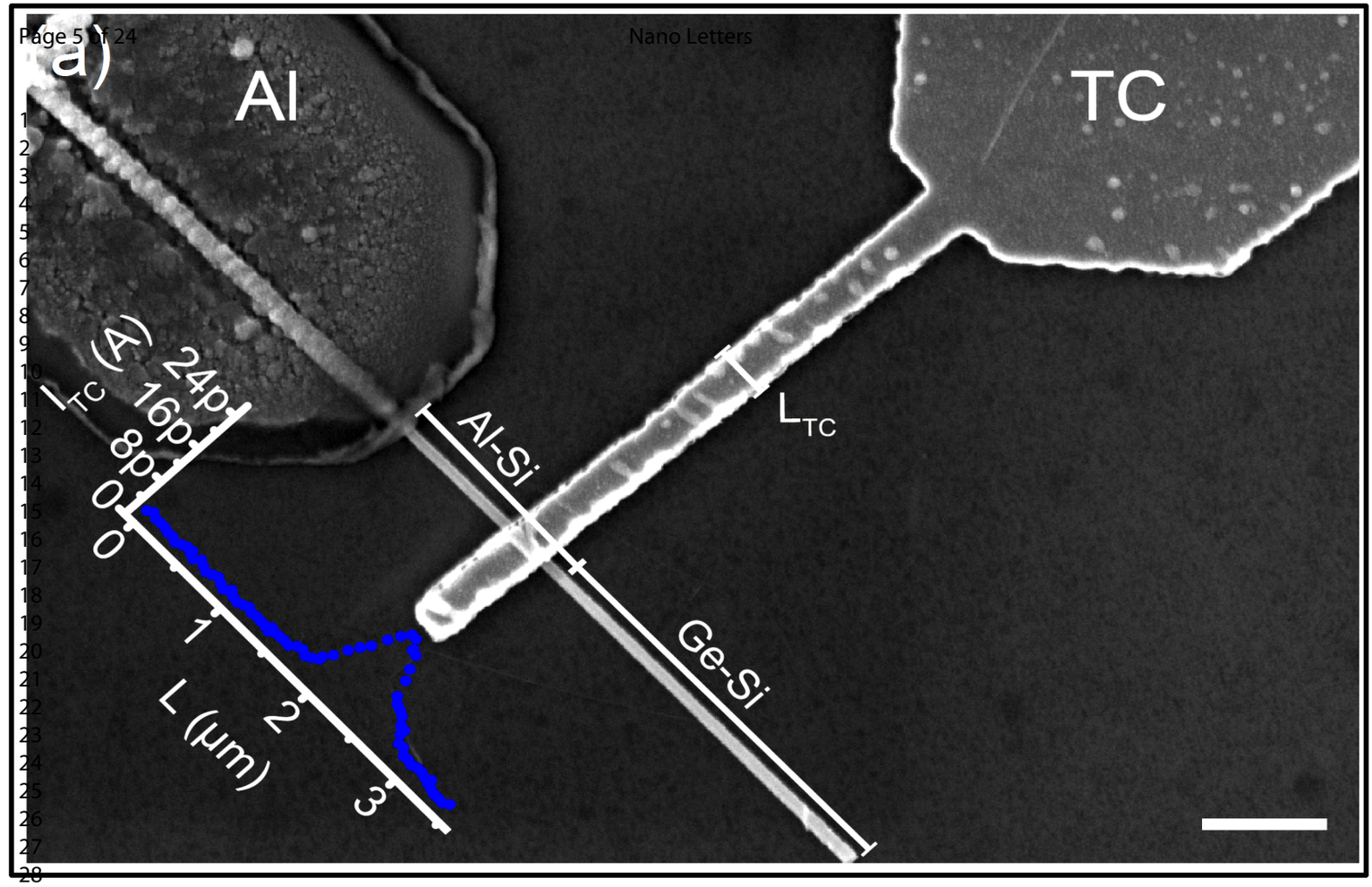
a)
Al
TC
I_{TC} (A)
24p
16p
8p
0
0
1
2
3
L (μm)
Al-Si
L_{TC}
Ge-Si

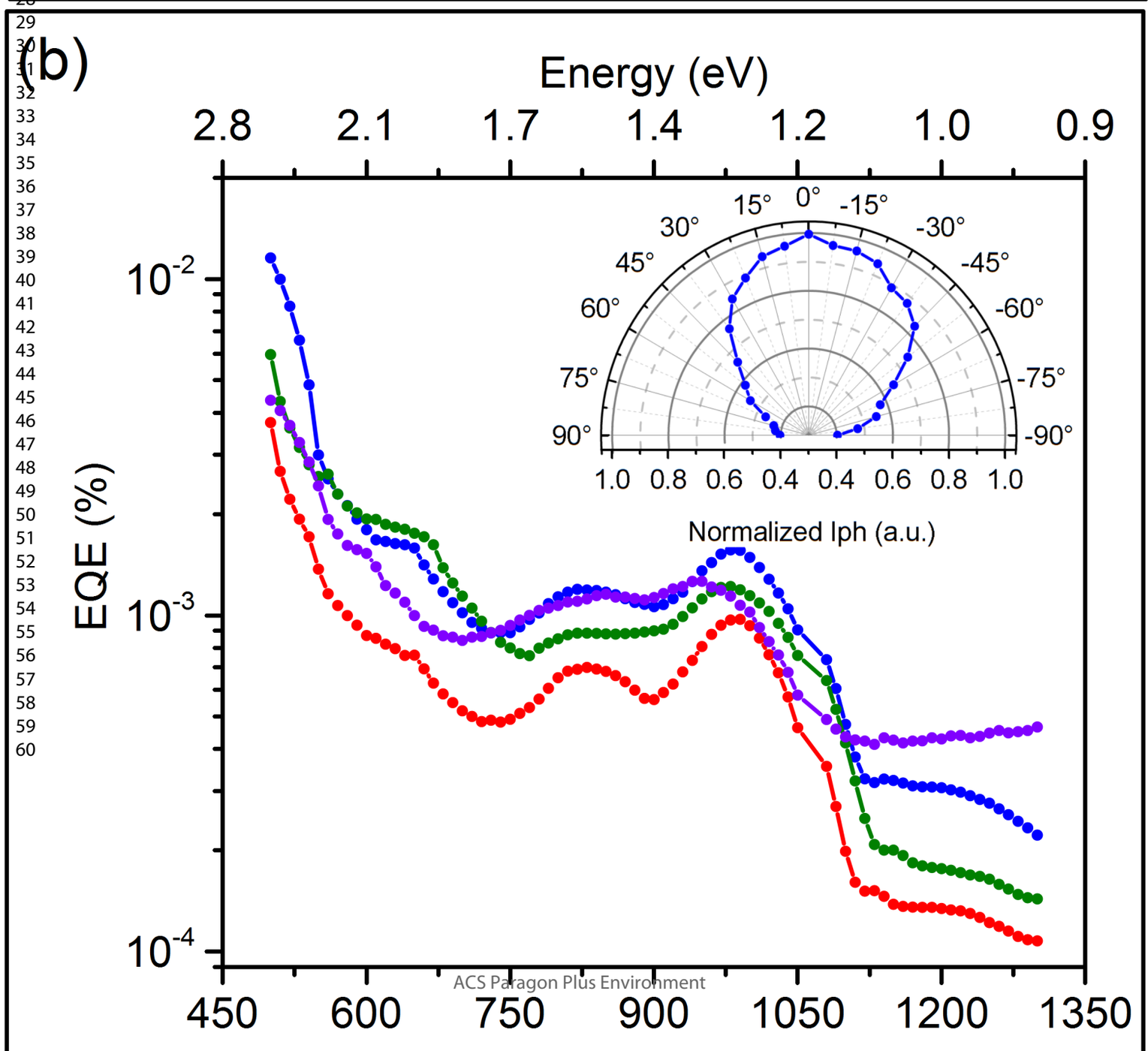
(b)
Energy (eV)
2.8
2.1
1.7
1.4
1.2
1.0
0.9
EQE (%)
10^{-2}
10^{-3}
10^{-4}
15°
0°
-15°
30°
-30°
45°
-45°
60°
-60°
75°
-75°
90°
-90°
1.0 0.8 0.6 0.4 0.4 0.6 0.8 1.0
Normalized Iph (a.u.)
450
600
750
900
1050
1200
1350

Monolithic axial and radial metal-semiconductor nanowire heterostructures

M. Sistani[1], M.A. Luong[2], M.I. den Hertog[3], E. Robin[2], M. Spies[3], B. Fernandez[3], J. Yao[4],

E. Bertagnolli[1], A. Lugstein[1]

[1] Institute of Solid State Electronics, Technische Universität Wien, Nanocenter Campus-Gußhaus, Gußhausstraße 25, Gebäude-CH, 1040 Vienna, Austria

[2] Univ. Grenoble Alpes, CEA, INAC, MEM, F-38000 Grenoble, France

[3] Univ. Grenoble Alpes, CNRS, Institut NEEL UPR2940, 25 avenue des Martyrs, 38042 Grenoble, France

[4] Department of Electrical and Computer Engineering, Institute for Applied Life Sciences, University of Massachusetts, Amherst, Massachusetts, 01003, USA.

KEYWORDS: nanowire, metal-semiconductor heterostructure, germanium, aluminum, transmission electron microscopy

The electrical and optical properties of low dimensional nanostructures depend critically on size and geometry and may differ distinctly from those of their bulk counterparts. In particular, ultra-thin semiconducting layers as well as nanowires have already proven the feasibility to realize and study quantum size effects enabling novel ultra-scaled devices. Further, plasmonic metal nanostructures attracted recently a lot of attention because of appealing near-field mediated enhancement effects. Thus, combining metal and semiconducting constituents in quasi 1D heterostructures will pave the way for ultra-scaled systems and high-performance devices with exceptional electrical, optical and plasmonic functionality.

This paper reports on the sophisticated fabrication and structural properties of axial and radial, Al-Ge and Al-Si nanowire heterostructures, synthesized by a thermally induced exchange reaction of single-crystalline Ge-Si core-shell nanowires and Al pads. This enables a self-aligned metallic contact formation to Ge segments beyond lithographic limitations as well as ultra-thin semiconducting layers wrapped around monocrystalline Al core nanowires. High-resolution transmission electron microscopy, energy dispersive X-ray spectroscopy and μ-Raman measurements proved the composition and perfect crystallinity of these metal-semiconductor nanowire heterostructures. This exemplary selective replacement of Ge by Al represents a general approach for the elaboration of radial and axial metal-semiconductor heterostructures in various Ge-semiconductor heterostructures.

The opportunity to tune the electrical and optical properties of nanostructures, which are distinctly different from those of their bulk counterparts, has motivated numerous scientific and practical approaches to manipulate matter on the nanometer scale.[1] In particular ultra-thin semiconducting layers as well as quasi 1D nanowires (NWs) have already proven the feasibility to realize and study quantum size effects enabling further novel ultra-scaled devices.[2,3,4] However, fabricating low resistive integrated contacts and interconnections is a crucial step towards the integration of reliable future ultra-scaled devices and requires sophisticated nanostructure formation techniques and precise lithography. So far, the large structural sizes of common extended contacts have been limiting the potential for scaling NW based devices.[5] Regarding this problematic, intense research on studying thermal induced diffusion processes of metals into Si and Ge NWs was carried out to form silicides and germanides respectively. In recent years, various materials including nickel,[6] cobalt,[7] platinum,[8] manganese,[9] and copper[10] have been investigated as diffusion sources. However, the resistivity of these quasi-metallic structures is still significantly higher compared to pure metals.[10,11] Moreover, radial epitaxy of dissimilar materials and multi-shell NWs[12] was pursued to explore the unique heterostructure-property functionality and interactions arising from the contributions of individual low-dimensional components unattainable in planar geometries.[6,7,8] With respect to photovoltaic applications, simulations revealed that the absorption in metal-semiconductor core-shell NWs can outperforms solid semiconductor NWs.[16] Further, a metal core will further facilitate the effective extraction of photo-generated carriers.[10,11] Moreover, metal nanostructures attracted a lot of attention because of appealing plasmonic effects on the near-field enhancement, which are anticipated as a potential solution for integrated on-chip photonic circuits that can combine both high operational speeds and ultra-compact architectures rivaling electronics in both speed and critical feature sizes.[12,13,14]

In this paper, the formation of such axial and radial metal-semiconductor nanowire heterostructures is based on vapor-liquid-solid (VLS)[22] grown core-shell NWs with a Ge NW core diameter of about 50 nm and a Si-shell thickness of about 3 nm. The metal core NW is formed by the substitution of the Ge core by crystalline Al (c-Al) utilizing a thermally induced exchange reaction. The principal mechanism and details of the processing are discussed in the paper of Kral et. al.[25] In contrast to the Cu-Ge[10] or Ni-Ge[23] systems forming germanides, no

such stable stoichiometric compound exists for the Al-Ge system.[24] We dedicate the exchange of Ge by Al to the asymmetric diffusion behavior present in the material system. While the diffusion of Ge in Al as well as self-diffusion of Al in Al is rather fast, the diffusion of Al in Ge is extremely slow.[26,27] Further, in contrast to the Kirkendall effect,[28] where lattice sites are being left behind when one element is diffusing faster than the others, in case of the Al-Ge system, Al is effectively supplied via fast self-diffusion and released to the Ge NW for the compensation of the Ge diffusion.[25] During our studies, we investigated different annealing temperatures. Effective exchange can be observed for temperatures above T = 624 K, however with a rather low rate of about 3 nm/s. With increasing temperature the exchange rate increases up to 20 nm/s at T = 685 K. For reliable heterostructure formation, we routinely perform the annealing process at 674 K resulting in an exchange rate of about 9 nm/s. Thus, adapting the contact spacing and reaction time, enables us to precisely tune the length of the Al leads and Ge-Si segment. An SEM image and a schematic illustration of the Ge-Si core-shell NW heterostructure with the Ge core partially substituted by c-Al are shown in figure 1a and 1b, respectively. Applying this heterostructure formation scheme allows the controlled and selective exchange of Ge by Al to fabricate both radial Al-Si core-shell NWs and axial Al-Ge-Al NW heterostructures enwrapped by a Si shell with tunable channel lengths beyond lithographic limitations.[29] For detailed analysis, high-resolution high angle annular dark field (HAADF) scanning transmission electron microscopy (STEM) at the Al-Ge interface (obtained at the yellow dashed square in figure 1a) oriented along the [11-2] direction of observation of the Ge crystal was performed (figure 1c). The contrast in HAADF STEM image in figure 1c is related to both the sample thickness and the mean atomic number. The thicker regions and/or those with a higher atomic number scatter more electrons on the annular detector and thus appear brighter in the HAADF STEM image. Since the diameter of VLS grown Ge-Si core-shell NW is quite uniform, the darker segment extending from the Al contact pads corresponds to the Al substituted part and the brighter segment to the unreacted Ge core part, separated by an atomically sharp metal-semiconductor interface. The inset of figure 1c shows the corresponding Fourier transformation (FT) of the image with indexed reflections in the Ge crystal and indicating the (111) reflection both in the Ge and c-Al part. Both the image and the FT show the (111) growth plane in the Ge diamond cubic structure with a lattice spacing of 0.33 nm, in good agreement with tabulated values.[30] In addition, the extra peak

indicated by the left arrow on the inset FT shows the presence of a family of planes with smaller lattice spacing of around 0.23 nm, which is in good agreement with the theoretical interplanar spacing of Al face centered cubic (fcc) for {111} planes.[31] The Al (111) plane is observed to be parallel to the Ge (111) growth plane, while the perpendicular reflection (2-20) is only visible in the Ge crystal, indicating that the Al crystal is not viewed along the same direction. Indeed, the Al crystal is rotated by ~6° around the NW axis with respect to the Ge crystal (image not shown) in this NW heterostructure. The interface appears to be very abrupt regardless of the large lattice mismatch between Al (a = 0.404 nm) and Ge (a = 0.565 nm) and no crystal defects are observed at the interface. Figure 1d also presents a high resolution HAADF STEM image at the Ge-Al reaction interface obtained near the NW surface, acquired along the [10-1] direction of observation, which represents a rotation of 30° around the NW axis with respect to the direction shown in Fig. 1c. The [10-1] direction of observation is confirmed by the FT indexed for the Ge crystal shown in the inset of Fig. 1d. Going from the NW core to the NW surface on the Al part, we see first a bright layer, surrounded by a darker layer, both of which share the lattice of the Ge part (atomic planes are visible). These layers are attributed respectively to a thin crystalline layer containing Ge as indicated by the arrow in figure 1d, surrounded by the Si shell outlined by dash-dotted lines. An amorphous layer is also observed around the crystalline Si shell, most likely consisting of SiO_2. The composition of these layers will be confirmed in the chemical analysis by energy dispersive x-ray spectroscopy (EDX) below. Moreover, the geometrical phase analysis (GPA)[20,21] on the Ge (2-20) reflection of the unreacted part of the NW oriented on the [11-2] direction, figure 1e-g, shows a decrease in lattice spacing at the sidewall, which is coherent with the smaller lattice spacing of Si (d_{220} = 0.192 nm). Clearly, the HRSTEM characterization confirms the presence of a uniform crystalline Si shell wrapped around the c-Al core NW.

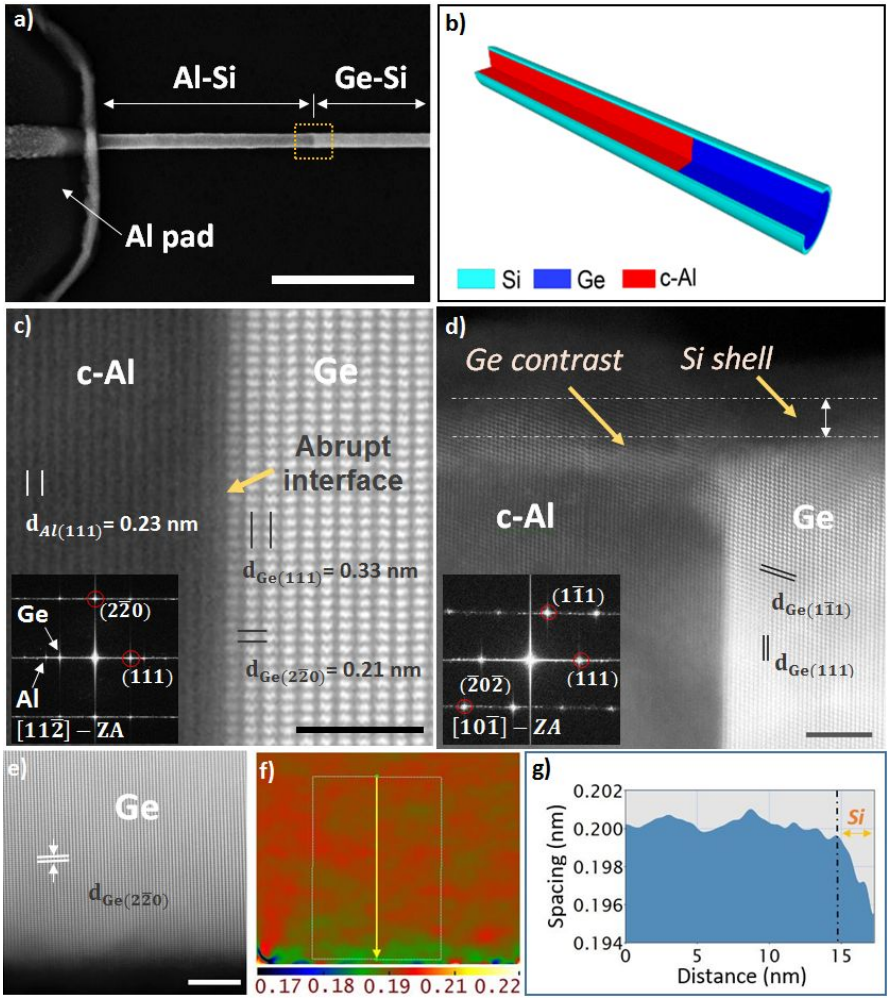

Figure 1. *(a) SEM image of a Ge-Si core-shell NW heterostructure with the Ge core NW partially substituted by c-Al. Scale bar is 1 μm. (b) Schematic illustration of the Al-Ge heterostructure with Si shell. (c) High-resolution HAADF STEM at the Al-Ge interface with corresponding Fourier transformation (FT) in the inset showing (111) planes in both Al and Ge parts with spacing's of 0.23 nm and 0.33 nm, respectively. Scale bar is 2 nm. (d) Zoom at the Al-Ge interface along another direction of observation with the corresponding FT in the inset indexed in the Ge part. The HAADF STEM contrast at the sidewall reveals the presence of an epitaxial shell wrapped around both the Ge as well as the c-Al core. Scale bar is 5 nm. (e-g) Geometrical phase analysis (GPA) along (2-20) planes in the unreacted Ge region shows a decrease in lattice spacing at the sidewall, which is coherent with the smaller lattice spacing in Si. Scale bar is 5 nm.*

To investigate the accurate composition of the NW heterostructure, energy dispersive X-ray spectroscopy (EDX) maps were acquired in STEM mode on the same sample, after the propagation of the c-Al phase inside the Ge-Si core-shell NW. Quantitative concentration profiles were extracted from the elemental maps allowing the reconstruction of the chemical nanostructure of both the unreacted and reacted parts of the NW (figure 2; see [34] and methods for details of the quantification and reconstruction procedure). The chemical reconstruction of the unreacted segment i.e. Ge-Si core-shell NW shows the presence of a 4 nm thick shell wrapped around the Ge core. The outer part of the shell is partly oxidized over 2 nm. A sharp SiGe interface of less than 2.5 nm is observed between the Si shell and the Ge core. The chemical reconstruction of the reacted segment also shows the presence of a Si shell, twice as thin as the previous one, whose outer part is also oxidized over 1 nm. We believe that the difference between the silicon oxide layer thickness of the reacted and unreacted part results from sample variations or the 3D reconstruction of the chemical maps obtained using EDX, which to increase the signal to noise in the radial profile were averaged along the diameter variations along the NW. Further, the reconstruction also reveals the presence of a 1.5 nm thick SiGe shell sandwiched between the Al core and the Si shell. One should also mention that prolonged thermal Ge-Al exchange leads finally to a complete exchange of the Ge by Al and thus to a uniform radial metal-semiconductor NW heterostructure. Thereby the diameter of the Al core NW and the thickness of the wrapped around semiconducting shell are inherited from the initial Ge-Si core-shell NW. Regarding the verification of the location of the Ge after the thermally induced exchange reaction, numerous EDX investigations following in-situ TEM experiments were conducted. Since for all investigated samples, pure and monocrystalline Al NWs with very low Ge concentrations present only in a shell region around the pure Al core were observed, we believe that the Ge diffuses in the extended Al contact-pads up to the solubility limit of 2%.[24]

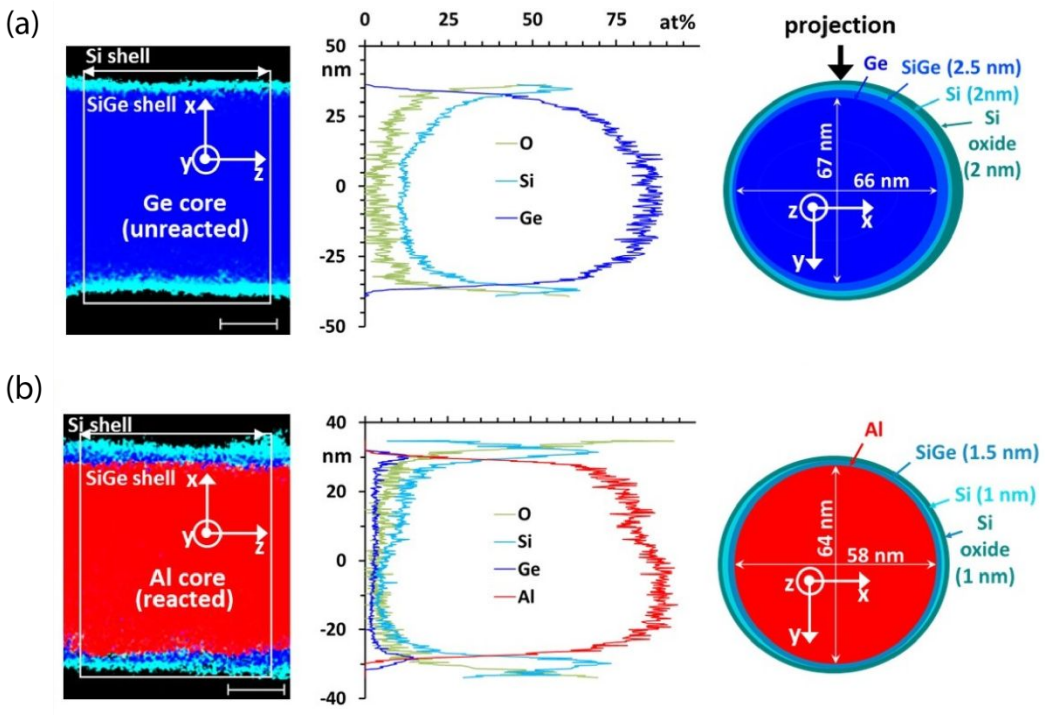

Figure 2. *Distribution of O, Al, Si and Ge measured by STEM/EDX in the (a) unreacted and (b) reacted Ge-Si core-shell NW heterostructure with partially substituted Ge core by c-Al. For each region we show from left to right the chemical map, the chemical profile in at. % obtained at the indicated location, as well as a model of the NW constructed by comparing the experimental quantified X-ray signal with a model, respectively. The vertical arrow indicates the projection direction of the model. The scale bars are 20 nm.*

Confocal μ-Raman spectroscopy (see methods) was employed to study the modification of the phonon spectra by quantum confinement effects in the ultra-thin semiconducting shell wrapped around the metallic Al core NW (figure 3a). For unambiguous Raman spectra interpretation, the core-shell NW heterostructures were fabricated on a 4H-SiC substrate, with the respective substrate peak at 203.5 cm^{-1}, far from the expected Raman signals of Ge and Si.[35] The Raman spectrum of the intrinsic Ge-Si core-shell NW (red) displays three distinct Raman transverse optical (TO) modes at 301, 405 and 475 cm^{-1} assigned to Ge-Ge vibrations in the Ge core NW, Ge-Si vibrations in the SiGe interlayer and Si-Si vibrations in the outermost Si shell, respectively.[24,25] The peak-broadening and frequency downshift of the first order Si-Si optical phonon mode from 520 cm^{-1} for bulk Si to 475 cm^{-1} is attributed to quantum confinement in the ultra-thin Si-shell.[26,27]

Figure 3b shows the polar representation of the normalized angle-dependent intensities of the Ge and Si related Raman signals for progressively rotating the excitation from transverse magnetic (TM) to transverse electric (TE) i.e. changing the electric field polarization from parallel to perpendicular to the NW axis. Both, the Ge NW core as well as the wrapped around ultra-thin Si shell exhibit the highest Raman intensity when the incident polarization is parallel to the NW axis. This enhanced response of the Raman scattering due to the anisotropy of NW geometry can be explained by considering the effect of the dielectric mismatch.[40]

The Raman spectrum after the thermal induced exchange of the Ge core (green spectrum in figure 3a) displays an enhanced background signal induced by the c-Al core NW. As expected, the peak at 301 cm^{-1} assigned to Ge disappeared proving complete exchange of the Ge core by Al. Further, the peak at 475 cm^{-1} associated to Si-Si TO vibrational modes increases and broadens. In accordance with the EDX analysis, which revealed a reduced shell thickness after the exchange reaction, we assume that a combination of surface enhanced Raman scattering[29,30] by the c-Al core and quantum confinement effects common for such ultra-thin layers[43] result in the aforementioned increase and broadening of the Si-Si TO vibrational mode. Even though the broad peak may overlap with a small Ge-Si related Raman peak, it confirms an intact Si shell wrapped around the c-Al core NW in accordance with EDX and TEM findings. The photo-response of such an ultra-thin Si-shell has been demonstrated by a wavelength dependent photocurrent measurement shown in the supporting information. Finally, as shown by the blue line in figure 3a, this peak disappears completely after extensive annealing in moderate vacuum, due to a complete oxidation of the ultra-thin Si shell. The overall enhanced broad background signal compared to the as grown core-shell NW (red spectrum) was reproducibly observed for fully exchanged NWs after prolonged annealing and is a signature of the c-Al NWs.

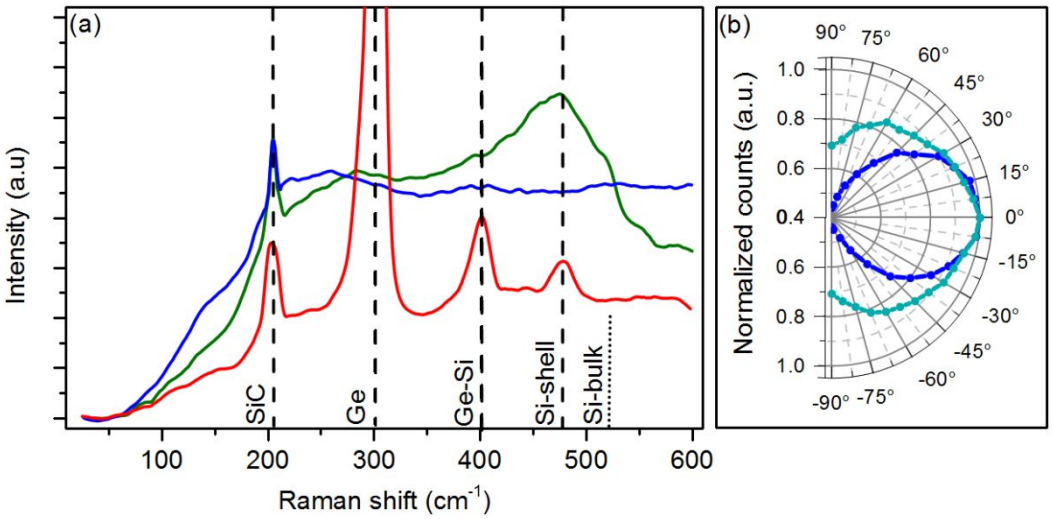

Figure 3. *(a) μ-Raman spectra of the core-shell NW heterostructure on a 4H-SiC substrate, measured on the Ge-Si core-shell segment (red) and the c-Al-Si core-shell segment (green). The blue spectrum corresponds to a fully exchanged and thus single crystalline Al NW after prolonged annealing and thus fully oxidized Si shell. To provide a reference, the position of the bulk Si peak is indicated at 520 cm^{-1}. (b) Polar representation of the normalized angle-dependent intensities of the peak at 301 cm^{-1} assigned to Ge core (blue) and the peak at 475 cm^{-1} assigned to the Si shell (cyan).*

In conclusion, this paper reports on the controlled formation and structural properties of axial and radial metal-semiconductor NW heterostructures. Comprehensive material analysis comprising HRSTEM measurements, EDX investigations and μ-Raman spectroscopy proved the composition and high crystallinity of the resultant NW nanostructures. For axial Al-Ge-Al NW heterostructures the length of the Ge segment can be tuned without lithographic limitations enabling investigations of quantum confinement effects in ultra-scaled semiconductors. With respect to the radial Al-Ge core-shell NW, we present the first experimental data of an ultra-scaled monocrystalline semiconducting layer wrapped around a crystalline metallic core NW paving the way for future ultra-scaled optoelectronic devices based on quasi 1D coaxial metal-semiconductor architectures. We assume that this selective replacement of Ge by Al, without limiting the

generality, represents an approach for the elaboration of radial and axial metal-semiconductor heterostructures in various Ge-semiconductor based systems.

METHODS:

Synthesis of monolithic axial and radial metal-semiconductor nanowire heterostructures:

The starting materials are VLS grown core-shell NWs with a Ge NW core diameter of 50 nm and a Si shell thickness of about 3 nm covered by a thin layer of native oxide.[44,45] The Ge-Si core-shell NWs were drop casted onto an oxidized highly p-doped Si substrate and the Ge core NW was contacted by Al pads fabricated by electron beam lithography, 100 nm Al sputter deposition and lift-off techniques. To gain access to the Ge core nanowire, the Si shell was selectively removed by wet chemical etching for 10 s in buffered HF (7:1) to remove the native oxide layer followed by 15 s in KOH (30%). A successive thermally induced exchange reaction by rapid thermal annealing at a temperature of T = 674 K in forming gas atmosphere initiates the substitution of the Ge core by c-Al.[25] Consecutive heating leads to a complete exchange of the Ge by Al and thus to a radial Al-Si NW heterostructure, where the core diameter and thickness of the Si-shell are inherited from the initial Ge-Si core-shell NW.

TEM measurements and STEM/EDX analysis:

For TEM investigations the fabrication was performed on dedicated Si_3N_4-TEM-membranes with holes, to obtain suspended and contacted NWs.[46] HAADF STEM was performed on a probe corrected FEI Titan Themis working at 200 kV equipped with four silicon drift detectors for energy dispersive X-ray (EDX) analysis. For EDX analysis we used a Fischione ultra narrow gap tomography sample holder. For high resolution imaging we used a DENSSolutions 6 contact double tilt holder. X-ray maps were acquired with a probe current of 340 pA. Scanning the probe for about 5 minutes over an area of 80x100 nm^2 using a pixel size of 0.25 nm, a dwell time of 45 µs per pixel, and drift correction activated. X-ray spectra were extracted from a 70-pixel-wide slice obtained normal to the NW axis for the reacted and unreacted

parts and a 50-pixel-wide slice made along the NW axis across the interface. Deconvolution and background subtraction of X-ray spectra were performed using the QUANTAX-800 software from BRUKER allowing extracting the net intensity of the characteristic X-rays (K-lines of O, Al, Si and Ge) generated by the elements present along the beam axis. Concentration and thickness profiles were determined using the zeta-factor method.[47] The absorption correction terms were estimated from a simple model[34] that takes into account the direction of the X-ray emission relative to the position of the detectors, knowing the thickness, density, and mass absorption coefficient of the material through which the radiations travel. Quantitative reconstructions of the cross-sections of the reacted and unreacted parts of the NW were performed by modelling the NW cross-section using a series of 4 imbricated ellipses whose dimensions and compositions were adjusted in such a way that the simulated profiles fit the experimental profiles (see [34] for details of the procedure for quantitative 3D reconstruction of a core-shell NW).

Methodology of Raman measurements:

For the Raman analysis, the core-shell NW heterostructures were fabricated on 4H-SiC substrates to eliminate interfering phonon contributions from the substrate. A confocal μ-Raman setup (Alpha300, WITec) was employed in backscattering geometry with a grating monochromator and a CCD camera (DV401-BV, Andor). As excitation source a frequency doubled Nd:YAG laser emitting linearly polarized light at λ = 532 nm is coupled to the system. The laser light passes a beam splitter with integrated polarizer and is focused on the sample surface through an achromatic Nikon EPI EPlan 100x objective (NA = 0.9, WD = 0.23 mm) enabling a diffraction limited spot size of ~720 nm. Except for the polarization depending measurements, the excitation laser was linearly polarized along the long axis of the NW, to optimize Raman signal intensity. The power of the laser was kept sufficiently low to avoid any shift in the phonon peaks due to laser-induced heating. The scattered light was again collected through the objective and filtered to remove the excitation wavelength and then coupled into a fiber, guiding the light to the spectrometer.

ASSOCIATED CONTENT

Supporting Information

Information supporting the discussion of photo-response of the ultra-thin Si-shell and wavelength dependent photocurrent measurements are provided.

Author Contributions

M.S. performed the device fabrication, experimental design, data analysis and wrote the manuscript. A.L. and E.B. conceived the project, contributed essentially to the experimental design and provided expertise on theoretical interpretations. M.I.H., L.M.A. and E.R. carried out the TEM and EDX measurements and analysis. M.Sp. and B.F. fabricated the Si_3N_4-TEM-membranes. J.Y. performed the synthesis of Ge-Si core-shell NWs and provided helpful feedback. All authors analysed the results and helped shape the research, analysis and manuscript.

Acknowledgements

The authors gratefully acknowledge financial support by the Austrian Science Fund (FWF): project No. P28175-N27. The authors further thank the Center for Micro- and Nanostructures for providing the cleanroom facilities. We acknowledge support from the Laboratoire d'excellence LANEF in Grenoble (ANR-10-LABX-51-01). Financial support from the ANR-COSMOS (ANR-12-JS10-0002) project is acknowledged. We acknowledge support from Campus France in the framework of PHC AMADEUS 2016 for PROJET N° 35592PB. We benefitted from the access to the Nano characterization platform (PFNC) in CEA Minatec Grenoble. Further, the authors very much appreciate the support by Charles M. Lieber, who commented on the manuscript and provided helpful feedback.

REFERENCES:

1. Lauhon, L. J., Gudiksen, M. S. & Lieber, C. M. Semiconductor nanowire heterostructures. *Philos. Trans. R. Soc. A Math. Phys.*

Eng. Sci. **362,** 1247–1260 (2004).

2. Zhao, X., Wei, C. M., Yang, L. & Chou, M. Y. Quantum Confinement and Electronic Properties of Silicon Nanowires. *Phys. Rev. Lett.* **92,** 236805 (2004).

3. Lin, L., Li, Z., Feng, J. & Zhang, Z. Indirect to direct band gap transition in ultra-thin silicon films. *Phys. Chem. Chem. Phys.* **15,** 6063 (2013).

4. Irrera, A. *et al.* Quantum confinement and electroluminescence in ultrathin silicon nanowires fabricated by a maskless etching technique. *Nanotechnology* **23,** 075204 (2012).

5. Neophytou, N., Jing Guo & Lundstrom, M. S. Three-dimensional electrostatic effects of carbon nanotube transistors. *IEEE Trans. Nanotechnol.* **5,** 385–392 (2006).

6. Wu, Y., Xiang, J., Yang, C., Lu, W. & Lieber, C. M. Single-crystal metallic nanowires and metal/semiconductor nanowire heterostructures. *Nature* **430,** 61–65 (2004).

7. Chou, Y.-C. *et al.* In-situ TEM observation of repeating events of nucleation in epitaxial growth of nano CoSi2 in nanowires of Si. *Nano Lett.* **8,** 2194–9 (2008).

8. Lin, Y.-C. *et al.* Single crystalline PtSi nanowires, PtSi/Si/PtSi nanowire heterostructures, and nanodevices. *Nano Lett.* **8,** 913–8 (2008).

9. Lin, Y.-C., Chen, Y., Shailos, A. & Huang, Y. Detection of Spin Polarized Carrier in Silicon Nanowire with Single Crystal MnSi as Magnetic Contacts. *Nano Lett.* **10,** 2281–2287 (2010).

10. Burchhart, T., Lugstein, A., Hyun, Y. J., Hochleitner, G. & Bertagnolli, E. Atomic Scale Alignment of Copper-Germanide Contacts for Ge Nanowire Metal Oxide Field Effect Transistors. *Nano Lett.* **9,** 3739–3742 (2009).

11. Liu, B., Wang, Y., Dilts, S., Mayer, T. S. & Mohney, S. E. Silicidation of Silicon Nanowires by Platinum. *Nano Lett.* **7,** 818–824 (2007).

12. Ray, S. K., Katiyar, A. K. & Raychaudhuri, A. K. One-dimensional Si/Ge nanowires and their heterostructures for multifunctional applications-a review. *Nanotechnology* **28,** 092001 (2017).

13. Heinzig, A., Slesazeck, S., Kreupl, F., Mikolajick, T. & Weber, W. M. Reconfigurable Silicon Nanowire Transistors. *Nano Lett.* **12,** 119–124 (2012).

14. Hyun, J. K., Zhang, S. & Lauhon, L. J. Nanowire Heterostructures. *Annu. Rev. Mater. Res.* **43,** 451–479 (2013).

15. Zheng, H., Li, Y., Liu, H., Yin, X. & Li, Y. Construction of heterostructure materials toward functionality. *Chem. Soc. Rev.* **40,** 4506 (2011).

16. Mann, S. A. & Garnett, E. C. Extreme Light Absorption in Thin Semiconductor Films Wrapped around Metal Nanowires. *Nano Lett.* **13,** 3173–3178 (2013).

17. Oener, S. Z. *et al.* Au-Cu2O core-shell nanowire photovoltaics. *Appl. Phys. Lett.* **106,** 023501 (2015).

18. Dai, X. *et al.* GaAs/AlGaAs Nanowire Photodetector. *Nano Lett.* **14,** 2688–2693 (2014).

19. Barnes, W. L., Dereux, A. & Ebbesen, T. W. Surface plasmon subwavelength optics. *Nature* **424,** 824–830 (2003).

20. Appenzeller, J. *et al.* Toward Nanowire Electronics. *IEEE Trans. Electron Devices* **55,** 2827–2845 (2008).

21. Geisler, P., Krauss, E., Razinskas, G. & Hecht, B. Transmission of Plasmons through a Nanowire. *ACS Photonics* **4,** 1615–1620 (2017).

22. Wagner, R. S. & Ellis, W. C. Vapor-liquid-solid mechanism of single crystal growth. *Appl. Phys. Lett.* **4,** 89–90 (1964).

23. Tang, J. *et al.* Formation and device application of Ge nanowire heterostructures via rapid thermal annealing. *Adv. Mater. Sci. Eng.* **2011,** (2011).

24. McAlister, A. J. & Murray, J. L. The Al-Ge (Aluminum-Germanium) system. *Bull. Alloy Phase Diagrams* **5,** 341–347 (1984).

25. Kral, S. *et al.* Abrupt Schottky Junctions in Al/Ge Nanowire Heterostructures. *Nano Lett.* **15,** 4783–7 (2015).

26. Beke, D. L. *Diffusion in Semiconductors*. **33A,** Springer-Verlag, 1998.

27. Gale, W. F. & Totemeier, T. C. *Smithells Metals Reference Book*. Elsevier Science, 2003.

28. Kirkendall, E. O. Diffusion of Zinc in Alpha Brass. *Trans. Metall. Soc. AIME* **147,** 104–109 (1942).

29. Sistani, M. *et al.* Room-Temperature Quantum Ballistic Transport in Monolithic Ultrascaled Al–Ge–Al Nanowire Heterostructures. *Nano Lett.* **17,** 4556–4561 (2017).

30. *D'Ans-Lax Taschenbuch für Chemiker und Physiker*. (Springer Berlin Heidelberg, 1998). doi:10.1007/978-3-662-01008-2

31. Jette, E. R. & Foote, F. Precision Determination of Lattice Constants. *J. Chem. Phys.* **3,** 605–616 (1935).

32. Hÿtch, M. J., Snoeck, E. & Kilaas, R. Quantitative measurement of displacement and strain fields from HREM micrographs. *Ultramicroscopy* **74,** 131–146 (1998).

33. Rouvière, J. L. & Sarigiannidou, E. Theoretical discussions on the geometrical phase analysis. *Ultramicroscopy* **106,** 1–17 (2005).

34. Rueda-Fonseca, P. *et al.* Quantitative Reconstructions of 3D Chemical Nanostructures in Nanowires. *Nano Lett.* **16,** 1637–1642 (2016).

35. Burton, J. C. *et al.* Spatial characterization of doped SiC wafers by Raman spectroscopy. *J. Appl. Phys.* **84,** 6268–6273 (1998).

36. Kodato, S. Si□Ge alloy film with very high electrical conductivity and thermoelectric power. *J. Non. Cryst. Solids* **77–78,** 893–896 (1985).

37. Young Lee, C. *et al.* Polycrystalline GexSi1 − x thin film formation by chemical vapor deposition using silicon difluoride and germanium tetrachloride as precursors. *J. Mater. Chem.* **11,** 687–690 (2001).

38. Faraci, G., Gibilisco, S., Pennisi, A. R. & Faraci, C. Quantum size effects in Raman spectra of Si nanocrystals. *J. Appl. Phys.* **109,** 074311 (2011).

39. Alonso, M. I. & Winer, K. Raman spectra of c - Si 1 − x Ge x alloys. *Phys. Rev. B* **39,** 10056–10062 (1989).

40. Wang, J. Highly Polarized Photoluminescence and Photodetection from Single Indium Phosphide Nanowires. *Science (80-.).* **293,** 1455–1457 (2001).

41. Campion, A. & Kambhampati, P. Surface-enhanced Raman scattering. *Chem. Soc. Rev.* **27,** 241 (1998).

42. Mogensen, K. B. *et al.* Surface-enhanced Raman scattering on aluminum using near infrared and visible excitation. *Chem. Commun.* **50,** 3744–3746 (2014).

43. Bruno, M., Palummo, M., Marini, A., Del Sole, R. & Ossicini, S. From Si Nanowires to Porous Silicon: The Role of Excitonic Effects. *Phys. Rev. Lett.* **98,** 036807 (2007).

44. Xiang, J., Vidan, A., Tinkham, M., Westervelt, R. M. & Lieber, C. M. Ge/Si nanowire mesoscopic Josephson junctions. *Nat. Nanotechnol.* **1,** 208–213 (2006).

45. Lu, W., Xiang, J., Timko, B. P., Wu, Y. & Lieber, C. M. One-dimensional hole gas in germanium/silicon nanowire heterostructures. *Proc. Natl. Acad. Sci.* **102,** 10046–10051 (2005).

46. den Hertog, M. *et al.* In situbiasing and off-axis electron holography of a ZnO nanowire. *Nanotechnology* **29,** 025710 (2018).

47. Watanabe, M. & Williams, D. B. The quantitative analysis of thin specimens: a review of progress from the Cliff-Lorimer to the new zeta-factor methods. *J. Microsc.* **221,** 89–109 (2006).